The Journal of Physical Chemistry Letters

Letter

Cite This: J. Phys. Chem. Lett. 2018, 9, 1990−1998

pubs.acs.org/JPCL

Li Distribution Heterogeneity in Solid Electrolyte $Li_{10}GeP_2S_{12}$ upon Electrochemical Cycling Probed by ^{7}Li MRI

Po-Hsiu Chien,[†,⊥] Xuyong Feng,[†,⊥] Mingxue Tang,[†,‡,⊥] Jens T. Rosenberg,[‡] Sean O'Neill,[†] Jin Zheng,[†] Samuel C. Grant,[‡,§] and Yan-Yan Hu*[,†,‡]

[†]Department of Chemistry and Biochemistry, Florida State University, Tallahassee, Florida 32306, United States

[‡]National High Magnetic Field Laboratory, 1800 East Paul Dirac Drive, Tallahassee, Florida 32310, United States

[§]Department of Chemical and Biomedical Engineering, FAMU-FSU College of Engineering, Tallahassee, Florida 32310, United States

Supporting Information

ABSTRACT: All-solid-state rechargeable batteries embody the promise for high energy density, increased stability, and improved safety. However, their success is impeded by high resistance for mass and charge transfer at electrode−electrolyte interfaces. Li deficiency has been proposed as a major culprit for interfacial resistance, yet experimental evidence is elusive due to the challenges associated with noninvasively probing the Li distribution in solid electrolytes. In this Letter, three-dimensional ^{7}Li magnetic resonance imaging (MRI) is employed to examine Li distribution homogeneity in solid electrolyte $Li_{10}GeP_2S_{12}$ within symmetric Li/$Li_{10}GeP_2S_{12}$/Li batteries. ^{7}Li MRI and the derived histograms reveal Li depletion from the electrode−electrolyte interfaces and increased heterogeneity of Li distribution upon electrochemical cycling. Significant Li loss at interfaces is mitigated via facile modification with a poly(ethylene oxide)/bis(trifluoromethane)sulfonimide Li salt thin film. This study demonstrates a powerful tool for noninvasively monitoring the Li distribution at the interfaces and in the bulk of all-solid-state batteries as well as a convenient strategy for improving interfacial stability.

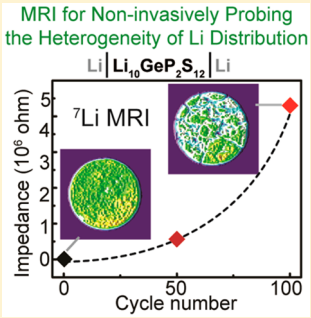

All-solid-state rechargeable batteries are promising for addressing the challenges faced by the current generation of liquid-electrolyte-based batteries, in areas of energy density, safety, and stability. Thanks to decades of research efforts, high-performance cathodes and anodes have been made available.[1−3] Fast alkali-ion conductors as electrolytes have realized ionic conductivities on the order of tens of mS/cm,[4−7] comparable to that for liquid electrolytes.[1] However, straightforward integration of high-performance electrodes and electrolytes does not necessarily produce high-performance all-solid-state batteries. The bottleneck lies at the electrode−electrolyte interfaces, including compatibility, stability, and thus the resulting high interfacial resistance for mass and charge transfer, which renders battery cells highly inefficient and often leads to performance failure during electrochemical cycling.[8,9] Therefore, major effort in developing all-solid-state rechargeable batteries is currently devoted to addressing issues associated with interfacial resistance.

The source of high interfacial resistance is believed to originate from structural mismatch of electrodes and solid electrolytes.[8,10] Further increase in interfacial resistance during electrochemical cycling is attributed to the formation of less conductive solid electrolyte interphases (SEIs).[11−13] Li deficiency at interfaces has also been proposed based on theoretical modeling;[14,15] however, experimental evidence is elusive due to the challenges in nondestructively probing the Li distribution within all-solid-state batteries.[16−22] In addition, Li concentration polarization within solid electrolytes may contribute to Li microstructure formation, leading to short circuits.[23−26] Therefore, the capability to follow the evolution of the Li distribution at interfaces and in the bulk of solid electrolytes is extremely important for establishing a correlation between Li deficiency and interfacial impedance and ultimately for addressing the major challenges in the development of high-performance all-solid-state batteries. Magnetic resonance imaging (MRI) is a powerful noninvasive tool to map out the distribution of chemical species and is widely employed in various areas of research.[27−29] In the studies of liquid-electrolyte-based rechargeable Li-ion batteries, ^{7}Li MRI was utilized to examine microstructure growth,[27,29−33] follow lithiation fronts,[28] and probe mass transport properties and Li concentration in the liquid electrolytes in operando.[34−38] Recently, Romanenko and co-workers reported the first quantitative in situ ^{1}H MRI study of operating solid-state Li-ion battery cells.[39] The obtained ^{1}H data was further correlated with the ^{7}Li density distribution with higher sensitivity compared with direct ^{7}Li MRI. In this Letter, we employ 3D ^{7}Li MRI to visualize the Li distribution in solid electrolytes and Li redistribution upon electrochemical cycling. The purpose of this study is to establish the correlation between Li deficiency and interfacial resistance in order to develop strategies for

Received: January 24, 2018
Accepted: March 29, 2018
Published: March 29, 2018

DOI: 10.1021/acs.jpclett.8b00240
J. Phys. Chem. Lett. 2018, 9, 1990−1998

mitigating Li concentration polarization and reducing interfacial resistance.

Li/$Li_{10}GeP_2S_{12}$/Li is chosen in this investigation for the following reasons: (1) $Li_{10}GeP_2S_{12}$ is a super ion conductor, with a high ionic conductivity of 12 mS/cm.[4] In the Li/$Li_{10}GeP_2S_{12}$/Li battery cell, the electrochemical impedance of the bulk electrolyte is negligible compared with interfacial resistance, making determination of the interfacial characteristics more convenient and reliable. (2) Due to large bulk ionic conductivity, it is possible to make thick electrolytes and probe the Li distribution within a large range of thicknesses. (3) $Li_{10}GeP_2S_{12}$ is not stable against Li metal, and decomposition products will form SEI layers; this provides the opportunity to distinguish the contribution of SEIs and Li deficiency toward interfacial resistance growth.

Further efforts have been made to mitigate Li concentration polarization and nonstable SEI formation by interface modification with a thin layer of polymer film.[40−42] As a result, the cell resistance and long-term stability are significantly improved. ^{7}Li MRI has been performed on this parallel system Li/PEO-coated $Li_{10}GeP_2S_{12}$/Li to further validate the correlation of interfacial resistance and Li deficiency established from the study on Li/$Li_{10}GeP_2S_{12}$/Li.

The synthesis of $Li_{10}GeP_2S_{12}$ is performed as described in the experimental section in the SI. To confirm the phase purity, determine the structure, and examine the surface morphology of $Li_{10}GeP_2S_{12}$ electrolytes, powder X-ray diffraction (XRD), solid-state NMR, and scanning electron microscopy (SEM) characterizations are performed, with results shown in Figure 1. The XRD pattern of the synthesized $Li_{10}GeP_2S_{12}$ matches the standard powder diffraction file[43] for $Li_{10}GeP_2S_{12}$ (Figure 1a), confirming the phase purity. The XRD pattern of PEO-coated $Li_{10}GeP_2S_{12}$ remains unchanged compared to that of pure $Li_{10}GeP_2S_{12}$, which suggests that, as expected, the PEO coating does not alter the bulk structure of $Li_{10}GeP_2S_{12}$. XRD provides long-range structural information, while NMR is sensitive to local structural modifications such as defect sites; thus, ^{7}Li and ^{31}P magic-angle spinning (MAS) NMR are employed to acquire more details on the structure of $Li_{10}GeP_2S_{12}$ and surface chemistry. The spectra are shown in Figures 1b,c and S1. ^{7}Li NMR of $Li_{10}GeP_2S_{12}$ with and without PEO coating shows a resonance at ∼1.8 ppm, suggesting a single Li local environment, consistent with the $Li_{10}GeP_2S_{12}$ structure.[44] ^{31}P NMR spectra exhibit two resonances at 93 and 75 ppm, which are assigned to P1 and P2 sites in the $Li_{10}GeP_2S_{12}$ structure, respectively.[44] Another resonance at 86 ppm comes from a minor structural modification that is commonly observed in $Li_{10}GeP_2S_{12}$.[44−46] Both ^{7}Li and ^{31}P NMR spectra are identical for $Li_{10}GeP_2S_{12}$ and PEO-coated $Li_{10}GeP_2S_{12}$. The evidence of the PEO coating is shown in the ^{1}H NMR spectrum (Figure S1), where a sharp ^{1}H resonance at ∼3.7 ppm from PEO is observed. The morphology of the $Li_{10}GeP_2S_{12}$ surface with and without PEO coating is probed using SEM. The SEM image of $Li_{10}GeP_2S_{12}$ in Figure 1d reveals a rough and porous surface, while that of PEO-coated $Li_{10}GeP_2S_{12}$ in Figure 1e exhibits an even and smooth surface. The thin layer of flexible PEO fills up the pores among $Li_{10}GeP_2S_{12}$ particles near the surface region (Figure 1e). In addition, the PEO layer is expected to isolate $Li_{10}GeP_2S_{12}$ from Li metal electrodes and thus to prevent chemical mixing, which will be discussed in more details in the following sections.

The electrochemical properties of $Li_{10}GeP_2S_{12}$ and PEO-coated $Li_{10}GeP_2S_{12}$ pellets are examined in symmetric solid-

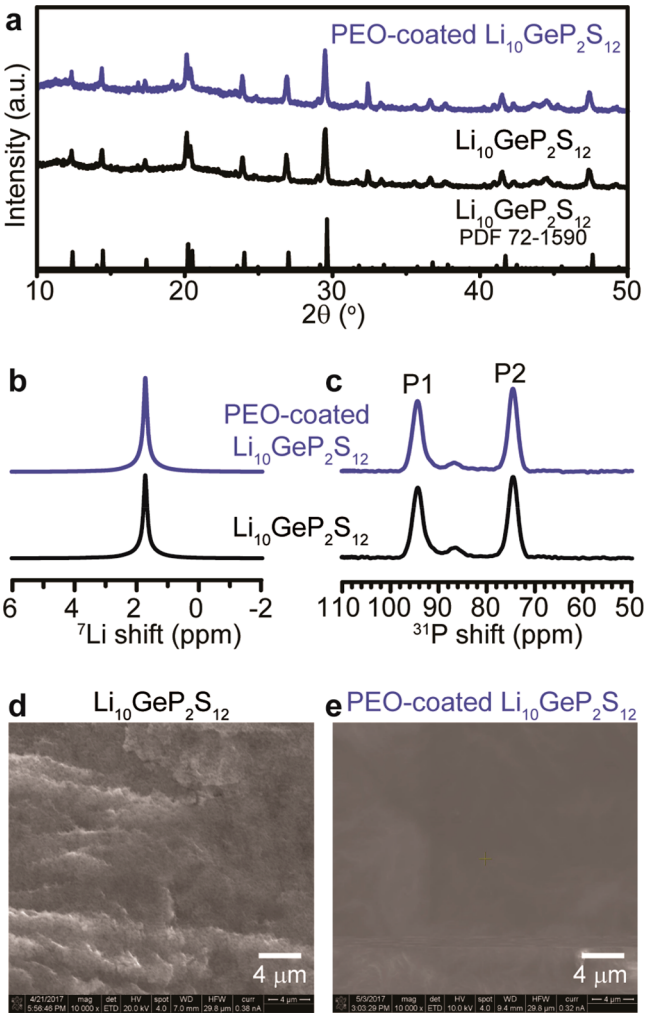

Figure 1. Characterizations of as-synthesized and PEO-coated $Li_{10}GeP_2S_{12}$ solid electrolyte pellets: (a) XRD. The standard powder diffraction file (PDF) of pure-phase $Li_{10}GeP_2S_{12}$ is shown at the bottom as a reference.[43] (b) ^{7}Li and (c) ^{31}P MAS NMR spectra. (d,e) SEM images.

state batteries using Li metal as electrodes (Figure 2a). Two pieces of Li foil are tightly pressed onto the two surfaces of the $Li_{10}GeP_2S_{12}$ pellet to make close contact. The electrochemically active components, Li/$Li_{10}GeP_2S_{12}$/Li or Li/PEO-coated $Li_{10}GeP_2S_{12}$/Li, are transferred into a homemade cylindrical cell designed for MRI.[30] The main body of the cylindrical cell (Figure 2b) is made of electrochemically inert polyether ether ketone (PEEK), which allows penetration of radio frequency (RF) pulses for NMR and MRI experiments. Highly pure stainless-steel wires and Cu foils are used as current collectors. Rubber O-rings are employed to ensure air-tightness. The assembled cylindrical battery cell is placed in a home-built low-*E* NMR probe[47] for enhanced sensitivity and minimized noise for NMR and MRI acquisitions. The following tests are performed by using the cylindrical cells, unless stated otherwise.

The electrochemical stability tests of $Li_{10}GeP_2S_{12}$ and PEO-coated $Li_{10}GeP_2S_{12}$ are performed, and the results are shown in Figure 3a. A constant electric current with a density of 20 μA/cm^2 is applied to Li/$Li_{10}GeP_2S_{12}$/Li and Li/PEO-coated $Li_{10}GeP_2S_{12}$/Li symmetric cells. The purpose of using a low current density of 20 μA/cm^2 is also to show that MRI is sensitive enough to follow small changes induced by small

DOI: 10.1021/acs.jpclett.8b00240
J. Phys. Chem. Lett. 2018, 9, 1990−1998

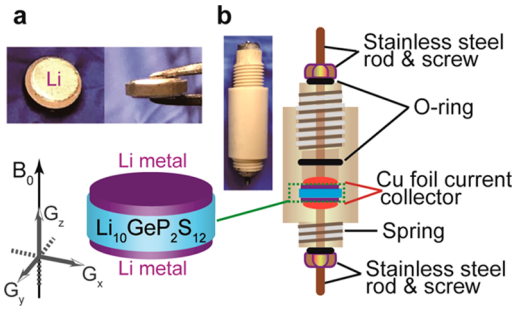

Figure 2. Pictures and schematic of a symmetric $Li/Li_{10}GeP_2S_{12}/Li$ battery placed in a home-made cylindrical cell for MRI. (a) Pictures (top and edge views) and schematic representation of the symmetric battery cell using Li metal as the electrode and $Li_{10}GeP_2S_{12}$ as the electrolyte. (b) Home-made cylindrical cell designed to host the $Li/Li_{10}GeP_2S_{12}/Li$ solid-state battery for MRI characterizations. The orientation of the battery relative to the external magnetic field $\mathbf{B}_0$ is shown. Field gradients are applied along the three orthogonal directions, G_x, G_y, and $G_z(\mathbf{B}_0)$.

currents. It is found that larger current densities will lead to more severe Li concentration polarization within a shorter time and thus a faster increase in cell impedance, which will be systematically discussed in our next paper. The direction of the current is changed every 1 h. A small cell voltage (<0.1 V) arises at the beginning as a result of nonvanishing cell resistance from bulk $Li_{10}GeP_2S_{12}$ and $Li/Li_{10}GeP_2S_{12}$ interfaces. The cell voltage of $Li/Li_{10}GeP_2S_{12}/Li$ shows a slight increase for the first 4 days (inset of Figure 3a), and then the increase rate picks up sharply. It reaches a very high voltage of 2.5 V after cycling for 9 days and results in battery failure (Figure 3a). In contrast, the cell voltage of Li/PEO-coated $Li_{10}GeP_2S_{12}/Li$ stays nearly constant, with only a very slight increase, and remains <0.25 V over an extended cycling period of 15 days. The Li/PEO-coated $Li_{10}GeP_2S_{12}/Li$ shows significantly improved long-term cycling stability compared to $Li/Li_{10}GeP_2S_{12}/Li$.

As the current density does not change, based on Ohm's law, $E = I{\cdot}R$, the increase in cell voltage is a reflection of cell resistance growth. The cell resistance is determined with electrochemical impedance spectroscopy (EIS). Figure 3b shows the EIS spectra of $Li/Li_{10}GeP_2S_{12}/Li$ and Li/PEO-coated $Li_{10}GeP_2S_{12}/Li$ pristine cells. A single semicircle is observed in the EIS spectra for the pristine $Li/Li_{10}GeP_2S_{12}/Li$ battery (Figure 3b) with an impedance of 1.3 kΩ, which is attributed to the interfacial resistance between Li metals and $Li_{10}GeP_2S_{12}$ electrolyte. The bulk resistance of $Li_{10}GeP_2S_{12}$ is too small, and the corresponding signature is buried within the same semicircle. Two semicircles are detected in the EIS spectra of the pristine Li/PEO-coated $Li_{10}GeP_2S_{12}/Li$ cell (Figure 3b). The first semicircle at high frequency is from the impedance of the thin PEO layer, which is much smaller compared with the impedance of a 40 μm thick PEO film (Figure S2). The second semicircle is associated with the total interfacial resistance between Li/PEO and $PEO/Li_{10}GeP_2S_{12}$, which is estimated to be 2.5 kΩ. As expected, the PEO coating increases interfacial resistance due to the formation of additional interfaces. The slightly increased resistance induced by PEO coating resulted in a higher initial cell voltage for Li/PEO-coated $Li_{10}GeP_2S_{12}/Li$ compared with that for $Li/Li_{10}GeP_2S_{12}/Li$ (inset in Figure 3a). It is worth mentioning that the interfacial resistance of $Li/Li_{10}GeP_2S_{12}$ increases from 1.3 to 6.0 kΩ within 30 min after assembly of the symmetric cell before the application of any electric current likely due to SEI formation (Figure S3). The bulk and interfacial impedance upon electrochemical cycling is also determined for both $Li_{10}GeP_2S_{12}$ and PEO-coated $Li_{10}GeP_2S_{12}$; the results are presented in Figure 3c. The bulk resistance does not vary significantly for either $Li_{10}GeP_2S_{12}$ or PEO-coated $Li_{10}GeP_2S_{12}$. The interfacial resistance for Li/PEO-coated $Li_{10}GeP_2S_{12}/Li$

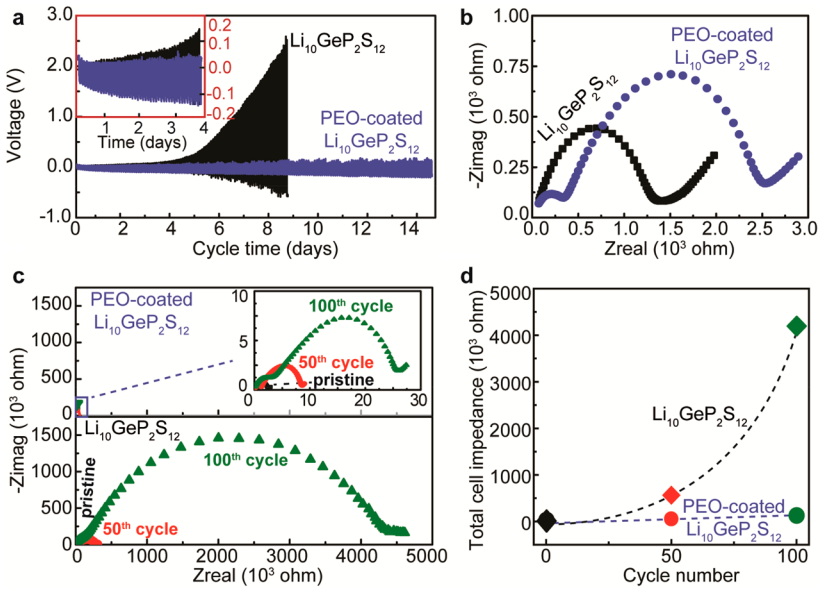

Figure 3. Long-term stability and electrochemical impedance spectroscopy (EIS) characterizations of symmetric $Li/Li_{10}GeP_2S_{12}/Li$ and Li/PEO-coated $Li_{10}GeP_2S_{12}/Li$ solid-state batteries. (a) Stability performance of $Li/Li_{10}GeP_2S_{12}/Li$ and Li/PEO-coated $Li_{10}GeP_2S_{12}/Li$ batteries. A constant current with a density of 20 $\mu A/cm^2$ is applied. The inset shows the amplification of the stability plots over the first 4 days. (b) EIS spectra of pristine $Li/Li_{10}GeP_2S_{12}/Li$ and Li/PEO-coated $Li_{10}GeP_2S_{12}/Li$ batteries and (c) the same two batteries after 50 and 100 cycles. The inset in (c) shows the amplification of the EIS spectra for the electrochemically cycled Li/PEO-coated $Li_{10}GeP_2S_{12}/Li$ battery. (d) Total cell impedance of the $Li/Li_{10}GeP_2S_{12}/Li$ and Li/PEO-coated $Li_{10}GeP_2S_{12}/Li$ batteries plotted as a function of cycle numbers.

DOI: 10.1021/acs.jpclett.8b00240
J. Phys. Chem. Lett. 2018, 9, 1990−1998

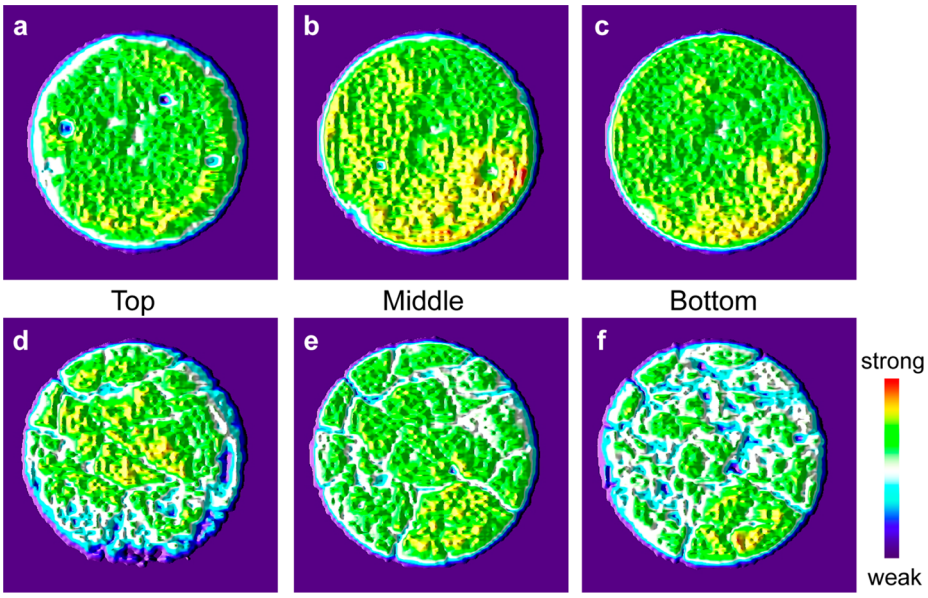

Figure 4. 2D cross sections taken from 3D ^{7}Li MRI images (Figures S8 and S9) of pristine and cycled $Li_{10}GeP_2S_{12}$ electrolytes in a symmetric Li/$Li_{10}GeP_2S_{12}$/Li cell. (a−c) Cross sections taken from the top, middle, and bottom, respectively, of the acquired 3D ^{7}Li MRI image of the pristine $Li_{10}GeP_2S_{12}$ pellet. (d−f) Corresponding cross sections of the $Li_{10}GeP_2S_{12}$ pellet after 3 days of electrochemical cycling. The color bar indicating the relative Li signal intensity is shown on the bottom right. The full set of the 2D cross sections is shown in the SI.

shows only a small increase with electrochemical cycling. The interfacial impedance of the Li/$Li_{10}GeP_2S_{12}$/Li cell is >150 times larger than that of the Li/PEO-coated $Li_{10}GeP_2S_{12}$/Li after 100 charge−discharge cycles. For a clear comparison of the magnitude in total resistance for the two cells, the resistance as a function of cycle numbers is plotted in Figure 3d. These data suggest that the increase in the cell total impedance is largely due to the growth of interfacial resistance between Li metal and $Li_{10}GeP_2S_{12}$ electrolytes. The interfacial impedance of the Li/$Li_{10}GeP_2S_{12}$/Li cell continues to increase after the cycling is ceased (Figure S6).

The impedance and electrochemical stability of the PEO-coated $Li_{10}GeP_2S_{12}$ is highly dependent on the thickness of the PEO coating and the amount of Lithium bis-(trifluoromethanesulfonyl)imide (LiTFSI) salt in PEO. Thicker PEO layers on the surface of $Li_{10}GeP_2S_{12}$ yield improved cycling stability but with a trade-off in initial impedance (Figure S4). The thickness of the PEO coating is varied with adjusting of the concentration of PEO solution. The 5 wt % PEO-coated $Li_{10}GeP_2S_{12}$ shows initial resistance of 0.44 and 2.94 kΩ from the PEO layer and electrode−electrolyte interfaces, respectively (Figure 3d). The corresponding resistance values for the 20 wt % PEO-coated $Li_{10}GeP_2S_{12}$ are 3.65 and 5.06 kΩ, respectively. After 50 cycles, both the PEO layer and electrode−electrolyte interface resistance increase 3-fold for the 5 wt % PEO-coated $Li_{10}GeP_2S_{12}$, while the corresponding resistance does not change significantly for the 20 wt % PEO-coated $Li_{10}GeP_2S_{12}$. With the same PEO content (e.g., 5 wt %), doubling the concentration of LiTFSI (EO/LiTFSI = 9:1) in PEO increases the ionic conductivity of the PEO layer but worsens the electrochemical stability (Figure S5).

Two possible reasons account for the fast increase in interfacial resistance: (i) the formation of less Li-conductive SEI layers and (ii) Li deficiency at electrode−electrolyte interfaces. To investigate the former, X-ray photoelectron spectroscopy (XPS) is employed to examine the surface of pristine and electrochemically cycled $Li_{10}GeP_2S_{12}$ pellets, and to probe Li deficiency, ^{7}Li MRI experiments are performed. The results are discussed in the following.

The XPS spectra of electrochemically cycled $Li_{10}GeP_2S_{12}$ and PEO-coated $Li_{10}GeP_2S_{12}$ are shown in Figure S7. Substantial formation of Li_2S is observed in cycled $Li_{10}GeP_2S_{12}$. S in Li_2S accounts for 13.5% of total S at the surface. Other studies also reported the formation of Li_2S, Li_3P, and Li_xGe_y due to the reactions between $Li_{10}GeP_2S_{12}$ and Li metal.[48,49] For PEO-coated $Li_{10}GeP_2S_{12}$, only 0.8% of S ends up in Li_2S after cycling and the XPS spectrum of the cycled pellet surface stays almost the same as pristine, indicating that the surface composition of the PEO-coated $Li_{10}GeP_2S_{12}$ is largely unchanged with cycling. The XPS results reveal that PEO coating helps to isolate Li from $Li_{10}GeP_2S_{12}$, and this isolation prevents undesirable chemical mixing at the interface.

To examine the Li redistribution within $Li_{10}GeP_2S_{12}$ and PEO-coated $Li_{10}GeP_2S_{12}$ pellets upon electrochemical cycling of the symmetric solid-state batteries, noninvasive ^{7}Li MRI experiments are performed at room temperature in a 21.1 T ultrawide bore magnet at the National High Magnetic Field Laboratory. Three-dimensional (3D) ^{7}Li MRI images of Li/$Li_{10}GeP_2S_{12}$/Li and Li/PEO-coated $Li_{10}GeP_2S_{12}$/Li solid-state battery cells have been acquired to follow the changes at both the interfaces and within the bulk of electrolytes. The Knight shift of Li metal is around 275 ppm, while the ^{7}Li signal from $Li_{10}GeP_2S_{12}$ electrolytes is at 1.8 ppm. The difference in shifts allows resolved imaging of Li from Li electrodes and $Li_{10}GeP_2S_{12}$. This work is mainly focused on the changes of the electrolyte; therefore, the transmitter frequency for ^{7}Li MRI acquisitions is set on the Li resonance of $Li_{10}GeP_2S_{12}$ at ∼1.8 ppm. The central axis of the cylindrical cell is aligned with the center of the external magnetic field $\mathbf{B}_0$. Magnetic field gradients are applied along three orthogonal directions, x, y, and z, as indicated in Figure 2. The 3D fast low-angle shot (FLASH) sequence is employed to acquire ^{7}Li MRI images of electrolyte pellets.

DOI: 10.1021/acs.jpclett.8b00240
J. Phys. Chem. Lett. 2018, 9, 1990−1998

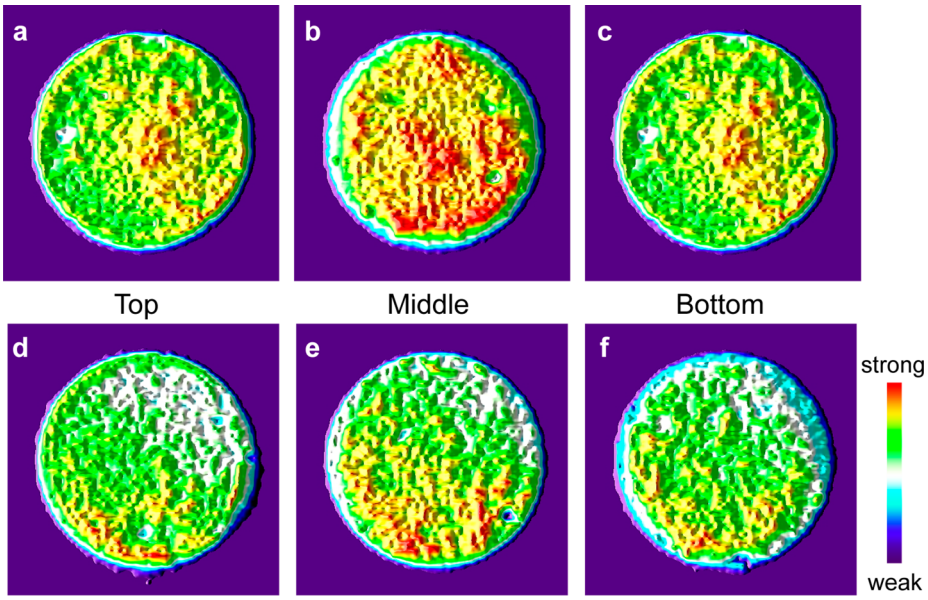

Figure 5. 2D cross sections taken from 3D ^{7}Li MRI images (Figures S8 and S9) of pristine and electrochemically cycled PEO-coated $Li_{10}GeP_2S_{12}$ electrolytes in a symmetric Li/PEO-coated $Li_{10}GeP_2S_{12}$/Li cell. (a−c) Cross sections taken from the top, middle, and bottom layers, respectively, of the acquired 3D ^{7}Li MRI image of the pristine PEO-coated $Li_{10}GeP_2S_{12}$ pellet. (d−f) Corresponding cross sections of the PEO-coated $Li_{10}GeP_2S_{12}$ pellet after 15 days of electrochemical cycling. The color bar shown on the bottom right indicates the relative Li signal intensity. The full set of 2D cross sections is shown in the SI.

To ensure that the ^{7}Li intensity in the MRI is proportional to Li concentration and the intensity map of ^{7}Li MRI directly reflects the Li distribution within the solid electrolytes, effects from T_1 contrast and magnetic susceptibility need to be investigated first. To eliminate possible T_1 contrast, preliminary experiments are carried out before MRI acquisitions to determine the minimum recycle delay for all of the resonances to fully relax after the flip pulse, which is found to be 1 s for both pristine and cycled $Li_{10}GeP_2S_{12}$ electrolytes. Therefore, the recycle delay is set to be 1 s. To further confirm that a 1 s recycle delay is sufficient, MRI images acquired with larger recycle delays than 1 s are acquired and shown in Figure S18, which exhibit no difference from the one acquired with a 1 s recycle delay. To correct for the magnetic susceptibility effects especially at the electrode−electrolyte interfaces, the following control experiments are performed. 2D ^{7}Li MRI images are acquired on the same $Li_{10}GeP_2S_{12}$ electrolyte pellet with and without Li metal on the surfaces, which are shown in Figure S19a,b, respectively. The sum of the ^{7}Li signal intensity for the top, middle, and bottom layers is surveyed, and the results show no significant difference for the same electrolyte pellet with and without Li metal attached (Figure S19c). Therefore, using MRI results to evaluate the relative total Li amount in different layers of the electrolyte pellet is reliable. However, the magnetic susceptibility effects of Li metal do lead to image distortion, especially around the edges of the cylindrical pellet, manifested as signal folding from the edge to the center, and this distortion is nearly the same for all of the layers, independent of their distances from the Li metal (Figure S19d). Therefore, analysis of the Li distribution homogeneity within the same layer needs to take into account this distortion.

3D ^{7}Li MRI images of $Li_{10}GeP_2S_{12}$ electrolytes before and after electrochemical cycling, with and without PEO coating, are shown in Figures S8−S10. Nine slices are generated by extracting 2D cross sections of the 3D MRI images with an equal spacing of ∼120 μm along the z-direction (Figure 2). Three representative slices are displayed in Figures 4 and 5 for $Li_{10}GeP_2S_{12}$ and PEO-coated $Li_{10}GeP_2S_{12}$, respectively: two slices extracted from the top and bottom of the electrolyte pellets in contact with Li foils and one slice from the center of the electrolytes. The rest of the 2D slices are displayed in Figures S13−S16.

The variation in Li concentration at electrode−electrolyte interfaces and the bulk $Li_{10}GeP_2S_{12}$ electrolyte before and after electrochemical cycling is manifested as changes in ^{7}Li MRI images shown in Figure 4. Figure 4a−c shows cross sections taken at the top, middle, and bottom layers from the 3D ^{7}Li MRI image of the $Li_{10}GeP_2S_{12}$ electrolyte pellet within a pristine Li/$Li_{10}GeP_2S_{12}$/Li cell, and the color map reflects the Li concentration gradient. The most Li-rich areas are coded in red and the most Li-deficient areas in blue. The sweeping color of green in the cross-sectional images of pristine $Li_{10}GeP_2S_{12}$ suggests a nearly homogeneous Li distribution. The yellow regions from the middle layer are Li-rich areas. The Li-rich regions are mainly observed in the center of the pellet, indicating higher Li density in the middle of the pellet compared with the bottom and top. It is a common phenomenon that solid electrolyte pellets are often slightly denser in the center than top/bottom surfaces. The slight heterogeneity in Li distribution is from the imperfect pellet manufacturing process, which can be potentially minimized with high-temperature press approaches.[50] The relative average Li density in each layer can be estimated based on the signal-to-noise (S/N) ratio of the ^{7}Li MRI images. The S/N ratios have been calculated for the top, middle, and bottom cross sections, and the values are listed in Table S1. On average, the middle of the pristine pellets is 20−25% denser than the top and bottom surface layers (Table S2). In the cross sections of the $Li_{10}GeP_2S_{12}$ electrolyte pellet after electrochemical cycling (Figure 4d−f), the ^{7}Li MRI cross sections reveal a heterogeneous ^{7}Li distribution and signs of cracking across the pellet. The degree of Li deficiency at electrode−electrolyte

DOI: 10.1021/acs.jpclett.8b00240
J. Phys. Chem. Lett. 2018, 9, 1990−1998

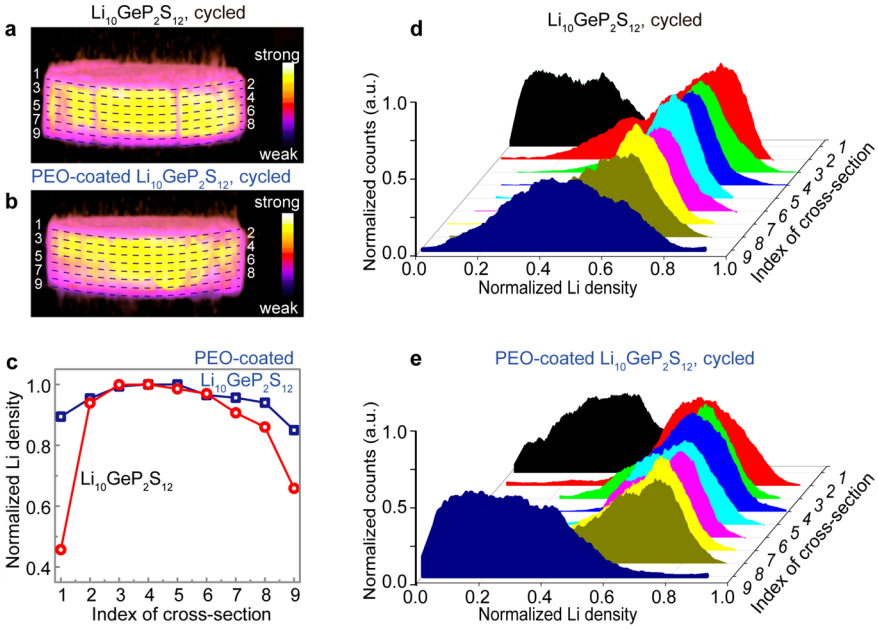

Figure 6. Li density profiles at different depths of electrochemically cycled $Li_{10}GeP_2S_{12}$ pellets. (a,b) ^{7}Li 3D MRI images of the electrochemically cycled $Li_{10}GeP_2S_{12}$ pellets without and with PEO coating. The color bars indicate the relative Li concentration, with yellow representing the Li density. (c) Normalized ^{7}Li densities across horizontal layers of the 3D electrolyte pellet plotted as a function of the layer index shown in (a,b). (d,e) Histograms of normalized Li density at different depths of the cycled $Li_{10}GeP_2S_{12}$ pellets shown in (a,b), respectively. The corresponding 3D MRI images and histograms for pristine $Li_{10}GeP_2S_{12}$ and PEO-coated $Li_{10}GeP_2S_{12}$ are shown in Figures S9 and S11.

interfaces can be evaluated by comparing the S/N ratios of top and bottom cross sections with that of the middle cross section. For instance, the S/N ratios for the top and bottom layers are only ∼58 and 82% of that for the middle layer, respectively (Tables S1 and S2). The asymmetry of Li deficiency at the top and bottom layers echoes the observed asymmetry in the overpotential in Figure 3a. Both top and bottom interfaces exhibit the formation of a SEI, cracking, and Li deficiency; however, the overpotential increase is only ∼0.5 V for one-direction cycling but >3.5 V for the other. This implies that the degree of Li deficiency is the major factor that determines the overpotential increase of all-solid-state batteries. To further prove this statement, the Li distribution homogeneity of the PEO-coated $Li_{10}GeP_2S_{12}$ before and after electrochemical cycling is also mapped out with ^{7}Li MRI (Figure 5). The 2D cross sections from the 3D MRI image of the PEO-coated $Li_{10}GeP_2S_{12}$ pellet before cycling (Figure 5a−c) shows varied signal intensities as reflected by the color map, suggesting Li distribution heterogeneity. The middle layer of the pellet is denser than the top and bottom layers revealed by the relative ^{7}Li signal intensity. After electrochemical cycling for 15 days, the homogeneity of the Li distribution within the PEO-coated $Li_{10}GeP_2S_{12}$ pellet is largely unchanged (Figure 5d−f), even though regional Li deficiency is observed in all layers of the pellet. Different from $Li_{10}GeP_2S_{12}$ pellets without PEO coating, no substantial variation in Li density from different layers is seen. For instance, the average S/N ratios of the top and bottom layers are ∼89 and 92% of that for the middle layer, respectively (Tables S1 and S2). As a result, the overpotential of the Li/PEO-coated $Li_{10}GeP_2S_{12}$/Li solid-state battery cell is relatively small and symmetric after cycling for 15 days (Figure 3).

As Li deficiency at electrode−electrolyte interfaces has been determined as the major source of interfacial resistance, the thickness of Li deficiency layers is surveyed more quantitatively and in more detail. Figure 6a,b present the edge view of the 3D ^{7}Li MRI images of $Li_{10}GeP_2S_{12}$ and PEO-coated $Li_{10}GeP_2S_{12}$ electrolyte pellets within symmetric battery cells after cycling. The color bars represent the relative Li signal intensity, with yellow indicating areas of highest Li concentration. The edge view of the 3D MRI images unveils Li deficiency at electrode−electrolyte interfaces. The histograms of the normalized Li concentration distribution within each layer for both electrochemically cycled $Li_{10}GeP_2S_{12}$ and PEO-coated $Li_{10}GeP_2S_{12}$ electrolyte pellets are shown in Figure 6c,d,e. The center of gravity for each histogram reflects the average Li concentration, and the spread is an indicator of Li distribution homogeneity. For the electrochemically cycled $Li_{10}GeP_2S_{12}$ pellet, the top and bottom layers show significant Li deficiency. Especially the top layer (Index 1) exhibits a large area of <10% Li content compared with areas of the highest Li concentration. The bottom layer (Index 9) also shows Li deficiency, manifested as the shift of the center of gravity by 15% compared with histograms from the center layers. Nevertheless, Li deficiency for the bottom layer is much less significant compared with that for the top layer. The wide spread of the histograms for both top and bottom layers indicates large Li distribution heterogeneity. The subsurface layers do not present signs of significant Li deficiency; however, the large width of the histograms implies increased heterogeneity. The histograms of the five middle layers do not exhibit notable differences, suggesting that the Li concentration distribution is nearly the same in the center. Compared with the histograms taken from the pristine $Li_{10}GeP_2S_{12}$ pellet (Figure S11), the peak width of the histogram plots for the $Li_{10}GeP_2S_{12}$ pellet after electrochemical cycling is nearly doubled, which is evidence for increased heterogeneity of the Li distribution induced by electrochemical cycling. For the electrochemically cycled PEO-coated $Li_{10}GeP_2S_{12}$ pellet, the shift in the mean values of the histograms for top and bottom layers compared with that for

DOI: 10.1021/acs.jpclett.8b00240
J. Phys. Chem. Lett. 2018, 9, 1990−1998

the middle layers infers Li deficiency at the electrode/electrolyte interfaces. Different from the cycled $Li_{10}GeP_2S_{12}$ pellet without PEO coating, Li deficiency of PEO-coated $Li_{10}GeP_2S_{12}$ is less significant and more symmetric for the top and bottom interfaces. Furthermore, smaller changes are observed for the surface layers. The average Li deficiency is further unveiled by the S/N ratios of the ^{7}Li signal in each layer plotted as a function of the layer index from top to bottom, as shown in Figure 6c. For the PEO-coated $Li_{10}GeP_2S_{12}$ pellet after electrochemical cycling, the S/N ratio does not vary notably except a slight drop by ∼10% for the top and bottom layers, while for cycled $Li_{10}GeP_2S_{12}$ without PEO coating, the S/N ratio is nearly 40% smaller for the top layer and 20% for the bottom. The decrease in S/N ratio goes beyond the surface layers and progresses into the subsurface layers for $Li_{10}GeP_2S_{12}$ without PEO coating (Figure 6c). In summary, quantitative analysis of the 3D ^{7}Li MRI reveals more severe Li deficiency at the surface and even in subsurface layers for $Li_{10}GeP_2S_{12}$ pellets after electrochemical cycling. This deficiency is asymmetric for the two surfaces, with the top showing ∼40% deficiency and 20% for the bottom. Only ∼10% Li deficiency is seen for top and bottom surfaces of the PEO-coated $Li_{10}GeP_2S_{12}$ pellet after cycling. No significant Li deficiency is observed in the bulk of the $Li_{10}GeP_2S_{12}$ or PEO-coated $Li_{10}GeP_2S_{12}$ pellet; however, the homogeneity of Li distribution is largely reduced across the whole electrolyte pellets after electrochemical cycling.

It is worth noting that Li deficiency probed by ^{7}Li MRI may be largely a reflection of chemical mixing in addition to the type of Li depletion that results in electric double-layer formation,[11−13] and the later plays a much more significant role in inducing an interfacial electric potential drop.[9] The PEO/LiTFSI layer at the electrode−electrolyte interfaces has multifold functions: (1) mitigation of loss in Li-ion concentration; (2) minimization of chemical mixing; and (3) provision of potential screening via mobile ions from LiTFSI.

The 3D ^{7}Li MRI studies of $Li/Li_{10}GeP_2S_{12}/Li$ symmetric batteries have revealed great Li loss at the $Li/Li_{10}GeP_2S_{12}$ interface upon electrochemical cycling. Li deficiency at the interface is determined to be the major cause for continuous increase in the interfacial resistance. The homogeneity of the Li distribution within the bulk of the solid electrolyte is also significantly compromised by electrochemical cycling, revealed by the more than doubled line width of Li density histograms and signs of Li vacant areas. Li concentration polarization in electrolytes has tremendous impact not only on cell resistance but also on Li microstructure formation and associated safety issues. Interfacial modification with a polymer film of appropriate thickness has tremendously improved Li distribution homogeneity at both the interface and bulk and thus enhanced the long-term cycling stability of all-solid-state battery cells. ^{7}Li MRI proves to be a nondestructive tool to follow the evolution of Li distribution upon electrochemical cycling, which will be invaluable for diagnosis of battery health and evaluations of novel strategies for improved battery performance.

■ ASSOCIATED CONTENT

Supporting Information

The Supporting Information is available free of charge on the ACS Publications website at DOI: 10.1021/acs.jpclett.8b00240.

Experimental details on sample preparation, characterizations, and additional NMR, impedance, XPS, and MRI data (PDF)

Movie of pristine LGPS (MPG)

Movie of cycled LGPS (MPG)

Movie of pristine PEO-coated LGPS (MPG)

Movie of cycled PEO-coated LGPS (MPG)

■ AUTHOR INFORMATION

Corresponding Author

*E-mail: hu@chem.fsu.edu.

ORCID

Po-Hsiu Chien: 0000-0002-1607-1271

Mingxue Tang: 0000-0002-7282-4100

Jin Zheng: 0000-0003-1114-1135

Yan-Yan Hu: 0000-0003-0677-5897

Author Contributions

⊥P.-H.C., X.F., and M.T. contributed equally, and their names are listed in alphabetical order. Y.-Y.H. designed and supervised the research project, X.F. and P.-H.C. synthesized the materials and performed XRD, SEM, and electrochemical characterizations, P.-H.C., M.T., and J.R. performed MRI measurements and data analysis with help from S.C.G. and Y.-Y.H., S.O. performed XPS measurements and data analysis with help from Y.-Y.H., P.-H.C. and J.Z. acquired NMR spectra, and Y.-Y.H. and M.T. wrote the manuscript with help from all of the coauthors.

Notes

The authors declare no competing financial interest.

■ ACKNOWLEDGMENTS

This work is supported by the National Science Foundation under Grant No. DMR-1508404. A portion of this work was performed at the National High Magnetic Field Laboratory, which is supported by National Science Foundation Cooperative Agreement No. DMR-1644779 and the State of Florida.

■ REFERENCES

(1) Tarascon, J.-M.; Armand, M. Issues and Challenges Facing Rechargeable Lithium Batteries. *Nature* **2001**, *414* (6861), 359−367.

(2) Magasinski, A.; Dixon, P.; Hertzberg, B.; Kvit, A.; Ayala, J.; Yushin, G. High-Performance Lithium-Ion Anodes Using a Hierarchical Bottom-up Approach. *Nat. Mater.* **2010**, *9* (4), 353−358.

(3) Larcher, D.; Tarascon, J.-M. Towards Greener and More Sustainable Batteries for Electrical Energy Storage. *Nat. Chem.* **2015**, *7* (1), 19−29.

(4) Kamaya, N.; Homma, K.; Yamakawa, Y.; Hirayama, M.; Kanno, R.; Yonemura, M.; Kamiyama, T.; Kato, Y.; Hama, S.; Kawamoto, K.; et al. A Lithium Superionic Conductor. *Nat. Mater.* **2011**, *10* (9), 682−686.

(5) Chu, I.-H.; Nguyen, H.; Hy, S.; Lin, Y.-C.; Wang, Z.; Xu, Z.; Deng, Z.; Meng, Y. S.; Ong, S. P. Insights into the Performance Limits of the $Li_7P_3S_{11}$ Superionic Conductor: A Combined First-Principles and Experimental Study. *ACS Appl. Mater. Interfaces* **2016**, *8* (12), 7843−7853.

(6) Kato, Y.; Hori, S.; Saito, T.; Suzuki, K.; Hirayama, M.; Mitsui, A.; Yonemura, M.; Iba, H.; Kanno, R. High-Power All-Solid-State Batteries Using Sulfide Superionic Conductors. *Nat. Energy* **2016**, *1* (4), 16030.

(7) Zheng, J.; Tang, M.; Hu, Y.-Y. Lithium Ion Pathway within $Li_7La_3Zr_2O_{12}$-Polyethylene Oxide Composite Electrolytes. *Angew. Chem., Int. Ed.* **2016**, *55* (40), 12538−12542.

(8) Han, X.; Gong, Y.; Fu, K.; He, X.; Hitz, G. T.; Dai, J.; Pearse, A.; Liu, B.; Wang, H.; Rubloff, G.; et al. Negating Interfacial Impedance in Garnet-Based Solid-State Li Metal Batteries. *Nat. Mater.* **2016**, *16* (5), 572−579.

DOI: 10.1021/acs.jpclett.8b00240
J. Phys. Chem. Lett. 2018, 9, 1990−1998

(9) Luntz, A. C.; Voss, J.; Reuter, K. Interfacial Challenges in Solid-State Li Ion Batteries. *J. Phys. Chem. Lett.* **2015**, *6* (22), 4599−4604.
(10) Luo, W.; Gong, Y.; Zhu, Y.; Fu, K. K.; Dai, J.; Lacey, S. D.; Wang, C.; Liu, B.; Han, X.; Mo, Y.; et al. Transition from Superlithiophobicity to Superlithiophilicity of Garnet Solid-State Electrolyte. *J. Am. Chem. Soc.* **2016**, *138* (37), 12258−12262.
(11) Wenzel, S.; Randau, S.; Leichtweiß, T.; Weber, D. A.; Sann, J.; Zeier, W. G.; Janek, J. Direct Observation of the Interfacial Instability of the Fast Ionic Conductor $Li_{10}GeP_2S_{12}$ at the Lithium Metal Anode. *Chem. Mater.* **2016**, *28* (7), 2400−2407.
(12) Han, F.; Zhu, Y.; He, X.; Mo, Y.; Wang, C. Electrochemical Stability of $Li_{10}GeP_2S_{12}$ and $Li_7La_3Zr_2O_{12}$ Solid Electrolytes. *Adv. Energy Mater.* **2016**, *6* (8), 1501590.
(13) Shin, B. R.; Nam, Y. J.; Oh, D. Y.; Kim, D. H.; Kim, J. W.; Jung, Y. S. Comparative Study of TiS_2/Li-In All-Solid-State Lithium Batteries Using Glass-Ceramic Li_3PS_4 and $Li_{10}GeP_2$ S_{12} Solid Electrolytes. *Electrochim. Acta* **2014**, *146*, 395−402.
(14) Yada, C.; Ohmori, A.; Ide, K.; Yamasaki, H.; Kato, T.; Saito, T.; Sagane, F.; Iriyama, Y. Dielectric Modification of 5V-Class Cathodes for High-Voltage All-Solid-State Lithium Batteries. *Adv. Energy Mater.* **2014**, *4*, 1301416.
(15) Moriwake, H.; Gao, X.; Kuwabara, A.; Fisher, C. A. J.; Kimura, T.; Ikuhara, Y. H.; Kohama, K.; Tojigamori, T.; Ikuhara, Y. Domain Boundaries and Their Influence on Li Migration in Solid-State Electrolyte $(La,Li)TiO_3$. *J. Power Sources* **2015**, *276*, 203−207.
(16) Liu, X. H.; Huang, J. Y. In Situ TEM Electrochemistry of Anode Materials in Lithium Ion Batteries. *Energy Environ. Sci.* **2011**, *4* (10), 3844−3860.
(17) Wen, R.; Hong, M.; Byon, H. R. In Situ AFM Imaging of Li−O_2 Electrochemical Reaction on Highly Oriented Pyrolytic Graphite with Ether-Based Electrolyte. *J. Am. Chem. Soc.* **2013**, *135* (29), 10870−10876.
(18) Aldon, L.; Perea, A. 2D-Correlation Analysis Applied to in Situ and Operando Mössbauer Spectroscopy. *J. Power Sources* **2011**, *196* (3), 1342−1348.
(19) Senyshyn, A.; Mühlbauer, M. J.; Nikolowski, K.; Pirling, T.; Ehrenberg, H. In-Operando" Neutron Scattering Studies on Li-Ion Batteries. *J. Power Sources* **2012**, *203*, 126−129.
(20) Hovington, P.; Dontigny, M.; Guerfi, A.; Trottier, J.; Lagacé, M.; Mauger, A.; Julien, C. M.; Zaghib, K. In Situ Scanning Electron Microscope Study and Microstructural Evolution of Nano Silicon Anode for High Energy Li-Ion Batteries. *J. Power Sources* **2014**, *248*, 457−464.
(21) Kirshenbaum, K.; Bock, D. C.; Lee, C.-Y.; Zhong, Z.; Takeuchi, K. J.; Marschilok, A. C.; Takeuchi, E. S. In Situ Visualization of Li/$Ag_2VP_2O_8$ Batteries Revealing Rate-Dependent Discharge Mechanism. *Science* **2015**, *347* (6218), 149−154.
(22) Pecher, O.; Carretero-González, J.; Griffith, K. J.; Grey, C. P. Materials' Methods: NMR in Battery Research. *Chem. Mater.* **2017**, *29* (1), 213−242.
(23) Harry, K. J.; Hallinan, D. T.; Parkinson, D. Y.; MacDowell, A. A.; Balsara, N. P. Detection of Subsurface Structures underneath Dendrites Formed on Cycled Lithium Metal Electrodes. *Nat. Mater.* **2014**, *13* (1), 69−73.
(24) Ren, Y.; Shen, Y.; Lin, Y.; Nan, C.-W. Direct Observation of Lithium Dendrites inside Garnet-Type Lithium-Ion Solid Electrolyte. *Electrochem. Commun.* **2015**, *57*, 27−30.
(25) Mauger, A.; Armand, M.; Julien, C. M.; Zaghib, K. Challenges and Issues Facing Lithium Metal for Solid-State Rechargeable Batteries. *J. Power Sources* **2017**, *353*, 333−342.
(26) Cheng, L.; Chen, W.; Kunz, M.; Persson, K.; Tamura, N.; Chen, G.; Doeff, M. Effect of Surface Microstructure on Electrochemical Performance of Garnet Solid Electrolytes. *ACS Appl. Mater. Interfaces* **2015**, *7* (3), 2073−2081.
(27) Chandrashekar, S.; Trease, N. M.; Chang, H. J.; Du, L.-S.; Grey, C. P.; Jerschow, A. ^{7}Li MRI of Li Batteries Reveals Location of Microstructural Lithium. *Nat. Mater.* **2012**, *11* (4), 311−315.
(28) Tang, M.; Sarou-Kanian, V.; Melin, P.; Leriche, J.-B.; Ménétrier, M.; Tarascon, J.-M.; Deschamps, M.; Salager, E. Following Lithiation Fronts in Paramagnetic Electrodes with in Situ Magnetic Resonance Spectroscopic Imaging. *Nat. Commun.* **2016**, *7*, 13284.
(29) Ilott, A. J.; Mohammadi, M.; Chang, H. J.; Grey, C. P.; Jerschow, A. Real-Time 3D Imaging of Microstructure Growth in Battery Cells Using Indirect MRI. *Proc. Natl. Acad. Sci. U. S. A.* **2016**, *113* (39), 10779−10784.
(30) Tang, J. A.; Dugar, S.; Zhong, G.; Dalal, N. S.; Zheng, J. P.; Yang, Y.; Fu, R. Non-Destructive Monitoring of Charge-Discharge Cycles on Lithium Ion Batteries Using ^{7}Li Stray-Field Imaging. *Sci. Rep.* **2013**, *3*, srep02596.
(31) Ilott, A. J.; Chandrashekar, S.; Klöckner, A.; Chang, H. J.; Trease, N. M.; Grey, C. P.; Greengard, L.; Jerschow, A. Visualizing Skin Effects in Conductors with MRI: 7Li MRI Experiments and Calculations. *J. Magn. Reson.* **2014**, *245*, 143−149.
(32) See, K. A.; Leskes, M.; Griffin, J. M.; Britto, S.; Matthews, P. D.; Emly, A.; Van der Ven, A.; Wright, D. S.; Morris, A. J.; Grey, C. P.; et al. Ab Initio Structure Search and in Situ ^{7}Li NMR Studies of Discharge Products in the Li−S Battery System. *J. Am. Chem. Soc.* **2014**, *136* (46), 16368−16377.
(33) Grey, C. P.; Tarascon, J. M. Sustainability and in Situ Monitoring in Battery Development. *Nat. Mater.* **2017**, *16* (1), 45−56.
(34) Klett, M.; Giesecke, M.; Nyman, A.; Hallberg, F.; Lindström, R. W.; Lindbergh, G.; Furó, I. Quantifying Mass Transport during Polarization in a Li Ion Battery Electrolyte by in Situ ^{7}Li NMR Imaging. *J. Am. Chem. Soc.* **2012**, *134* (36), 14654−14657.
(35) Krachkovskiy, S. A.; Pauric, A. D.; Halalay, I. C.; Goward, G. R. Slice-Selective NMR Diffusion Measurements: A Robust and Reliable Tool for In Situ Characterization of Ion-Transport Properties in Lithium-Ion Battery Electrolytes. *J. Phys. Chem. Lett.* **2013**, *4* (22), 3940−3944.
(36) Sethurajan, A. K.; Krachkovskiy, S. A.; Halalay, I. C.; Goward, G. R.; Protas, B. Accurate Characterization of Ion Transport Properties in Binary Symmetric Electrolytes Using In Situ NMR Imaging and Inverse Modeling. *J. Phys. Chem. B* **2015**, *119*, 12238−12248.
(37) Krachkovskiy, S. A.; Bazak, J. D.; Werhun, P.; Balcom, B. J.; Halalay, I. C.; Goward, G. R. Visualization of Steady-State Ionic Concentration Profiles Formed in Electrolytes during Li-Ion Battery Operation and Determination of Mass-Transport Properties by in Situ Magnetic Resonance Imaging. *J. Am. Chem. Soc.* **2016**, *138* (25), 7992−7999.
(38) Chang, H. J.; Ilott, A. J.; Trease, N. M.; Mohammadi, M.; Jerschow, A.; Grey, C. P. Correlating Microstructural Lithium Metal Growth with Electrolyte Salt Depletion in Lithium Batteries Using ^{7}Li MRI. *J. Am. Chem. Soc.* **2015**, *137* (48), 15209−15216.
(39) Romanenko, K.; Jin, L.; Howlett, P.; Forsyth, M. In Situ MRI of Operating Solid-State Lithium Metal Cells Based on Ionic Plastic Crystal Electrolytes. *Chem. Mater.* **2016**, *28* (8), 2844−2851.
(40) Zhang, Z.; Zhao, Y.; Chen, S.; Xie, D.; Yao, X.; Cui, P.; Xu, X. An Advanced Construction Strategy of All-Solid-State Lithium Batteries with Excellent Interfacial Compatibility and Ultralong Cycle Life. *J. Mater. Chem. A* **2017**, *5* (32), 16984−16993.
(41) Zhang, W.; Nie, J.; Li, F.; Wang, Z. L.; Sun, C. A Durable and Safe Solid-State Lithium Battery with a Hybrid Electrolyte Membrane. *Nano Energy* **2018**, *45*, 413−419.
(42) Kaneko, M.; Nakayama, M.; Wakizaka, Y.; Kanamura, K.; Wakihara, M. Enhancement of Electrochemical Ion/Electron-Transfer Reaction at Solid‖liquid Interface by Polymer Coating on Solid Surface. *Electrochim. Acta* **2008**, *53* (28), 8196−8202.
(43) Kuhn, A.; Köhler, J.; Lotsch, B. V. Single-Crystal X-Ray Structure Analysis of the Superionic Conductor $Li_{10}GeP_2S_{12}$. *Phys. Chem. Chem. Phys.* **2013**, *15* (28), 11620−11622.
(44) Kuhn, A.; Duppel, V.; Lotsch, B. V. Tetragonal $Li_{10}GeP_2S_{12}$ and Li_7GePS_8 − Exploring the Li Ion Dynamics in LGPS Li Electrolytes. *Energy Environ. Sci.* **2013**, *6* (12), 3548−3552.
(45) Berman, M. B.; Greenbaum, S. G. NMR Studies of Solvent-Free Ceramic Composite Polymer Electrolytes—A Brief Review. *Membranes* **2015**, *5* (4), 915−923.
(46) Liang, X.; Wang, L.; Jiang, Y.; Wang, J.; Luo, H.; Liu, C.; Feng, J. In-Channel and In-Plane Li Ion Diffusions in the Superionic

DOI: 10.1021/acs.jpclett.8b00240
J. Phys. Chem. Lett. 2018, 9, 1990−1998

Conductor $Li_{10}GeP_2S_{12}$ Probed by Solid-State NMR. *Chem. Mater.* **2015**, *27* (16), 5503−5510.

(47) Fu, R.; Brey, W. W.; Shetty, K.; Gor'kov, P.; Saha, S.; Long, J. R.; Grant, S. C.; Chekmenev, E. Y.; Hu, J.; Gan, Z.; et al. Ultra-Wide Bore 900 MHz High-Resolution NMR at the National High Magnetic Field Laboratory. *J. Magn. Reson.* **2005**, *177* (1), 1−8.

(48) Ong, S. P.; Mo, Y.; Richards, W. D.; Miara, L.; Lee, H. S.; Ceder, G. Phase Stability, Electrochemical Stability and Ionic Conductivity of the $Li_{10\pm1}MP_{2\times12}$ (M = Ge, Si, Sn, Al or P, and X = O, S or Se) Family of Superionic Conductors. *Energy Environ. Sci.* **2013**, *6* (1), 148−156.

(49) Wang, Y.; Richards, W. D.; Ong, S. P.; Miara, L. J.; Kim, J. C.; Mo, Y.; Ceder, G. Design Principles for Solid-State Lithium Superionic Conductors. *Nat. Mater.* **2015**, *14* (10), 1026−1031.

(50) Kim, Y.; Jo, H.; Allen, J. L.; Choe, H.; Wolfenstine, J.; Sakamoto, J. The Effect of Relative Density on the Mechanical Properties of Hot-Pressed Cubic $Li_7La_3Zr_2O_{12}$. *J. Am. Ceram. Soc.* **2016**, *99* (4), 1367−1374.

DOI: 10.1021/acs.jpclett.8b00240
J. Phys. Chem. Lett. 2018, 9, 1990−1998